Sound radiation due to boundary layer transition

By Meng Wang

1. Motivation and objectives

This report describes progress made to date towards calculations of noise produced by the laminar-turbulence transition process in a low Mach number boundary layer formed on a rigid wall. The primary objectives of the study are to elucidate the physical mechanisms by which acoustic waves are generated, to clarify the roles of the fluctuating Reynolds stress and the viscous stress in the presence of a solid surface, and to determine the relative efficiency as a noise source of the various transition stages. In particular, we will examine the acoustic characteristics and directivity associated with three-dimensional instability waves, the detached high-shear layer, and turbulent spots following a laminar breakdown. Additionally, attention will be paid to the unsteady surface pressures during the transition, which provide a source of flow noise as well as a forcing function for wall vibration in both aeronautical and marine applications.

Interest in flow transition as a potential noise source stems from the transient nature of the transition process (Farabee *et al.* 1989). A clear understanding of the phenomena has so far been elusive due to fundamental difficulties associated with the strong nonlinear effects in the Navier-Stokes equation system. For this reason, rigorous analytical studies are mostly concerned with the early, linear stages of transition. For instance, Tam & Morris (1980) and Akylas & Toplosky (1986) examined the sound emitted by linear instability wave packets in a plane shear layer and a laminar boundary layer, respectively, by using multiple-scale perturbation techniques. The analysis of Haj-Hariri & Akylas (1986), although weakly nonlinear, is limited to slightly supercritical Reynolds numbers so that the unstable disturbance is only weakly amplified. Because of the small amplification rate for linear Tollmien-Schlichting (T-S) waves in a boundary layer, the associated sound field is typically of very small magnitude.

An alternate approach for studying flow induced sound is the theory due to Lighthill (1952), which provides a formal expression for the linear acoustic field driven by equivalent source terms representing the nonlinear turbulent fluctuations in a spatially concentrated region. The theory, also known as acoustic analogy, is essentially a rearrangement of the exact equations for mass and momentum conservation into a wave equation form. The driving terms on the right hand side are assumed known *a priori* rather than treated as part of the solution, thus simplifying the problem tremendously. For compact flows at low Mach number, this assumption can be viewed as a leading order approximation to the fully coupled acoustic-fluid dynamic system. By using the method of matched asymptotic expansions based on small Mach number, Crow (1970) shows that Lighthill's solution is adequate for sound emission from compact eddy regions. More recently, Mitchell

et al. (1993) tested Lighthill's theory and its extensions against solutions computed directly from the compressible Navier-Stokes equations, for the case of the merger of two co-rotating vortices. Excellent agreement has been obtained.

To predict the emitted sound using acoustic analogy theories, one requires knowledge of the source region, or the unsteady flow field. Traditionally, the source terms are approximated by empirical correlations based on experimental measurements. The rapid development in CFD applications in recent years has made it possible to compute the transitional and turbulent flow quantities directly by solving the full Navier-Stokes equations, thus allowing a more detailed assessment of the acoustic source. With the currently available supercomputers, direct numerical simulations (DNS) for controlled boundary layer transition can be carried out up to the laminar breakdown stage (see, for example, Zang and Hussaini 1990; Kleiser & Zang 1991; Fasel 1990). This has motivated us to undertake the present work, focusing on acoustic processes during boundary layer transition. By combining a DNS approach for the source region with modeling efforts based on Lighthill's theory, we attempt to reveal the sound production features during the transition process, in parameter ranges not accessible previously.

2. Accomplishments

2.1 Formulation

The continuity and momentum equations for a compressible flow above a flat surface can be combined to generate, in dimensionless form,

$$\left[\left(\frac{\partial}{\partial t}+M\frac{\partial}{\partial X_1}\right)^2-\frac{\partial^2}{\partial X_j\partial X_j}\right]\rho=\frac{\partial^2\rho}{\partial x_1^2}-2\frac{\partial^2(\rho u_j)}{\partial x_1\partial x_j}+\frac{\partial^2 T_{ij}}{\partial x_i\partial x_j}, \tag{1}$$

where

$$T_{ij}=\rho u_i u_j+\frac{\delta_{ij}}{M^2}\left(\frac{p}{\gamma}-\rho\right)-\tau_{ij} \tag{2}$$

is called Lighthill's stress tensor. It contains the Reynolds stress (the term is used in a generalized sense since $\rho u_i u_j$ contains both mean and fluctuating velocities), deviation from isentropy (the second term), and the viscous part of the Stokes stress tensor

$$\tau_{ij}=\frac{1}{Re}\left(\frac{\partial u_i}{\partial x_j}+\frac{\partial u_j}{\partial x_i}-\frac{2}{3}\delta_{ij}\frac{\partial u_k}{\partial x_k}\right). \tag{3}$$

In (1)–(3), the velocity components and the thermodynamic variables are nondimensionalized with respect to the undisturbed free-stream values U'_∞, p'_∞, ρ'_∞, and T'_∞, respectively. The spatial variables are defined by $x_i = x'_i/L'_f$, where L'_f is a characteristic length scale of the flow field such as the boundary layer displacement thickness and $X_i = Mx_i$. The latter, resembling the outer scale in matched asymptotic expansions, is introduced here to facilitate the description of far field acoustic propagation. We will be using x_i and X_i simultaneously to represent the near-field source region and the far-field observation points, respectively, bearing in mind that

they are not independent of one another. The nondimensional time, $t = t'U'_\infty/L'_f$, is the same for both acoustic and fluid dynamic disturbances. The Mach number is defined in terms of the equilibrium sound speed in the free stream, $M = U'_\infty/c'_\infty$; $c'_\infty = (\gamma p'_\infty/\rho'_\infty)^{\frac{1}{2}}$, and the Reynolds number is defined as $Re = U'L'_f/\nu'$.

Eqn. (1) is equivalent to a convective wave equation for a medium moving uniformly along the X_1 axis, if the right hand side is viewed as distributed source terms. In the spirit of Lighthill's theory, we treat the right hand side as pure fluid dynamic quantities confined within the thin boundary layer and decoupled from acoustic disturbances, on the basis that the latter are much smaller in magnitude. Thus, the flow noise issue is reduced to a problem of finding the solution to (1) under the appropriate boundary conditions once the flow field in known.

For a low Mach number flow, the proper scales for the thermodynamic variables in the boundary layer are

$$p = 1 + M^2\tilde{p}, \qquad \rho = 1 + M^2\tilde{\rho}, \qquad T = 1 + M^2\tilde{T}. \tag{4}$$

It can be easily shown that the governing equations for an ideal gas have the following form:

$$\frac{\partial u_j}{\partial x_j} = O(M^2), \tag{5}$$

$$\frac{\partial u_i}{\partial t} + u_j\frac{\partial u_i}{\partial x_j} = -\frac{1}{\gamma}\frac{\partial \tilde{p}}{\partial x_i} + \frac{1}{Re}\frac{\partial^2 u_i}{\partial x_j \partial x_j} + O(M^2), \tag{6}$$

$$\frac{\partial \tilde{s}}{\partial t} + u_j\frac{\partial \tilde{s}}{\partial x_j} = \frac{1}{PrRe}\frac{\partial^2 \tilde{s}}{\partial x_j \partial x_j} + \frac{1}{PrRe}\left(\frac{\gamma - 1}{\gamma}\right)\frac{\partial^2 \tilde{p}}{\partial x_j \partial x_j} + \frac{\gamma - 1}{Re}\Phi + O(M^2), \tag{7}$$

where the entropy $\tilde{s} = \tilde{p}/\gamma - \tilde{\rho}$ is exactly the second term in Lighthill's stress tensor. Eqns. (5)–(7) suggest that for low Mach number flows, one only needs to solve the incompressible version of the governing equations in order to evaluate the acoustic source terms with reasonable accuracy. In fact, the first two terms in the forcing function in (1) can be ignored because they are of $O(M^2)$ (cf. (4) and (5)). The density in the Reynolds stress terms in (2) can be replaced by 1. The viscous stress terms in T_{ij}, on the other hand, must be retained at the moment even though they appear to be $O(M^2)$. As will become clear later, viscous stress tends to form dipoles on the solid wall that are efficient acoustic radiators.

The effect of entropy change on sound production deserves special comments. Although it is customary to ignore it entirely in the application of Lighthill's theory, there is no clear justification for doing so in a transitional boundary layer, based upon the above analysis. Eqn. (7) implies that the entropy production can be quantified by solving a passive-scalar type of equation together with the incompressible Navier-Stokes equations, rather than resorting to a fully compressible code. It would be of interest to pursue this issue in a future endeavor. In the present work, however, we will focus on the Reynolds stress and viscous stress contributions to sound production, assuming that the entropy effect is relatively small.

If the $O(M)$ effect of bulk flow convection is ignored, (1) becomes the Lighthill equation in a uniform acoustic medium at rest. Its solution in the upper half space $X_2 \geq 0$ can be written as (Crighton *et al.* 1992)

$$4\pi\left[\rho(\vec{X},t)-1\right] = M^5 \frac{\partial^2}{\partial X_i \partial X_j}\int_{V_0} \frac{T_{ij}(\vec{y},t-|\vec{X}-M\vec{y}|)}{|\vec{X}-M\vec{y}|}dV(\vec{y}) + M^5 \frac{\partial^2}{\partial X_i^* \partial X_j^*}\int_{V_0} \frac{T_{ij}(\vec{y},t-|\vec{X}^*-M\vec{y}|)}{|\vec{X}^*-M\vec{y}|}dV(\vec{y}) - 2M^4 \frac{\partial}{\partial X_\alpha}\int_{S_0} \frac{\tau_{\alpha 2}(\vec{y},t-|\vec{X}-M\vec{y}|)}{|\vec{X}-M\vec{y}|}dS(\vec{y}), \tag{8}$$

where $\vec{X}^* = (X_1, -X_2, X_3)$ is the image of the position $\vec{X}$ in the rigid surface $X_2 = 0$, and unlike indices i and j, α takes the values of 1 and 3 only. The volume integrations are to be carried out throughout the entire source region, and the surface integral should be evaluated on the wall. The three terms on the right hand side of (8) represent, respectively, a volume distribution of acoustic quadrupoles, reflection on the rigid surface, and a surface distribution of viscous dipoles. It should be noted that the dipole term has a coefficient $O(M^{-1})$ times larger than that for the quadrupole terms, and hence it is not necessarily negligible despite the apparent smallness of τ_{ij}.

Under the assumption that the unsteady flow region is small in comparison to the emitted acoustic wavelengths (compact source), (8) can be approximated by

$$4\pi\left[\rho(\vec{X},t)-1)\right] = M^5 \frac{X_i X_j + X_i^* X_j^*}{|\vec{X}|^3}\left[\frac{\partial^2}{\partial t^2}Q_{ij}(t-|\vec{X}|) + \frac{3}{|\vec{X}|}\left(1+\frac{\partial}{\partial t}\right)Q_{ij}(t-|\vec{X}|)\right] + 2M^4 \frac{X_\alpha}{|\vec{X}|^2}\left[\frac{\partial}{\partial t}R_\alpha(t-|\vec{X}|) + \frac{1}{|\vec{X}|}R_\alpha(t-|\vec{X}|)\right] \tag{9}$$

The quadrupole and dipole sources are

$$Q_{ij}(t) = \int_{V_0} T_{ij}(\vec{y},t)dV(\vec{y}), \qquad R_\alpha(t) = \int_{S_0} \tau_{\alpha 2}(\vec{y},t)dS(\vec{y}). \tag{10}$$

They do not contain the retarded potential as in (8) and are, therefore, straightforward to evaluate. In the far field, $|\vec{X}| \gg 1$, only the first term in the two square brackets in (9) are of importance.

It is sometimes of interest to calculate the sound field caused by a two-dimensional boundary layer. A two-dimensional version of (8)–(10) has been derived by the method of descent, *i.e.*, by integrating (8) along the Y_3 axis from $-\infty$ to $+\infty$,

noting that the source properties are independent of Y_3. For brevity, only the far field solution for a compact source is presented here:

$$\pi\left[\rho(\vec{X},t)-1\right] = M^4\frac{X_1^2}{|\vec{X}|^2}\int_0^\infty \frac{1}{\cosh^2(\xi)}\frac{\partial^2}{\partial t^2}Q_{11}\left(t-|\vec{X}|\cosh(\xi)\right)d\xi + M^4\frac{X_2^2}{|\vec{X}|^2}\int_0^\infty \frac{1}{\cosh^2(\xi)}\frac{\partial^2}{\partial t^2}Q_{22}\left(t-|\vec{X}|\cosh(\xi)\right)d\xi + M^3\frac{X_1}{|\vec{X}|}\int_0^\infty \frac{1}{\cosh(\xi)}\frac{\partial}{\partial t}R_1\left(t-|\vec{X}|\cosh(\xi)\right)d\xi. \tag{11}$$

The quantities Q_{11}, Q_{22}, and R_1 are surface and line integrals defined as

$$Q_{ij}(t) = \int_{S_0} T_{ij}(\vec{y},t)dS(\vec{y}), \qquad R_1(t) = \int_{C_0} \tau_{12}(\vec{y},t)dC(\vec{y}). \tag{12}$$

A similar solution without the solid boundary effect has been obtained by Mitchell *et al.* (1993), using a Green's function approach.

2.2 Numerical method and boundary conditions

In order to evaluate the acoustic source terms associated with boundary layer transition, (5) and (6) are solved using an incompressible Navier-Stokes solver developed by Le and Moin (1991). The equations are discretized using finite difference on a staggered grid, with uniform grid spacing in the streamwise (x_1) and spanwise (x_3) directions. In the wall-normal direction (x_2), non-uniform mesh is employed to allow grid refinement near the plate. Time advancement is of predictor-corrector type combined with a fractional step method. Each time step treats the convective terms explicitly and the viscous terms implicitly. The pressure is calculated by solving the Poisson equation. The numerical scheme is second order accurate in both space and time.

The domain of integration consists of a rectangular box that covers 5–10 streamwise Tollmien-Schlichting wavelengths in x_1 and one spanwise wavelength in x_3. The distance from the wall to the free-stream boundary is equal to 20 times the inflow displacement thickness. A no-slip boundary condition is applied at the solid wall. At the free-stream boundary, a normal velocity distribution based on the Blasius solution is imposed; in addition, the vorticity is assumed to be negligible there. In the x_3 direction, periodicity is assumed of all dependent variables.

The inflow boundary conditions for the simulations are of the form

$$u_i(x_1=0) = Real\Big\{u_i^B(x_2) + \epsilon^{2D}u_i^{2D}(x_2)e^{i\theta}e^{-i\beta t} + \frac{1}{2}\epsilon^{3D}u_i^{3D+}(x_2)e^{i[(\alpha\sin\phi)x_3-\beta t]} + \frac{1}{2}\epsilon^{3D}u_i^{3D-}(x_2)e^{i[-(\alpha\sin\phi)x_3-\beta t]}\Big\} \tag{13}$$

where $u_i^B(x_2)$ represents the Blasius solution for a 2-D boundary layer. $u_i^{2D}(x_2)$ and $u_i^{3D\pm}(x_2)$ are the least stable linear modes of the Orr-Sommerfeld (Squire) equation for given frequency β and oblique angle ϕ. The eigenfunctions are normalized such that the maximum streamwise velocity has a magnitude of 1. Since we are primarily interested in laminar breakdown of the fundamental type, the same excitation frequency is applied to both the 2-D and 3-D disturbances. For 2-D calculations, one simply ignores the 3-D terms in (13).

At the outflow boundary, an ideal boundary condition must allow smooth passage of disturbance structures while maintaining the correct mean velocity profile. The convective boundary condition

$$\frac{\partial u_i}{\partial t} + U\frac{\partial u_i}{\partial x_1} = 0 \tag{14}$$

is frequently used for this purpose (see Pauley *et al.* (1988) for an extensive discussion), where U is the mean exit velocity. When tested for the case of 2-D T-S waves, however, the normal velocity u_2 exhibits point-to-point oscillations in both mean and disturbance quantities (Fig. 1a). In addition, the mean velocity deviates significantly from the true value (the top curve in Fig. 1b) near the exit boundary $x_1 = 50$. Errors for the streamwise velocity u_1 have the same absolute magnitude as for u_2, but are less prominent in relative terms. These errors occur because of unphysical boundary layers formed along the exit plane, which are not resolved properly on the given grid (Johansson 1993).

An improvement has been made by replacing (14) with

$$\frac{\partial u_i}{\partial t} + U_j\frac{\partial u_i}{\partial x_j} = U_j\frac{\partial u_i^B}{\partial x_j} \tag{15}$$

where u_i^B is the Blasius solution and U_j denotes the characteristic velocity at the exit plane. $U_j = (1, 0, 0)$ for calculations presented in the present work. Eqn. (15) ensures that the steady solution converges to the laminar velocity profile while disturbances are allowed to be convected out of the domain. For turbulence simulations, u_i^B should be replaced by the appropriate mean profiles, perhaps through an iterative procedure.

One way to remove the wiggles in the disturbance velocities is by grid refinement near the outflow boundary so that the unphysical boundary layer can be resolved. This is, however, expensive and often impractical. The method adopted in this study is to employ a small buffer zone consisting of 5 to 10 grid points next to the exit boundary. In this zone, the velocity field is filtered at each integration step using an explicit, three-point low pass filter. As can be observed in Fig. 1b, this expedient approach removes the wiggles quite effectively. Since the buffer zone is very small and located in the downstream direction, its impact on the overall computational solution is expected to be negligible.

The time-dependent code is shown to be capable of producing and maintaining steady state solutions that are in excellent agreement with the Blasius solution. It

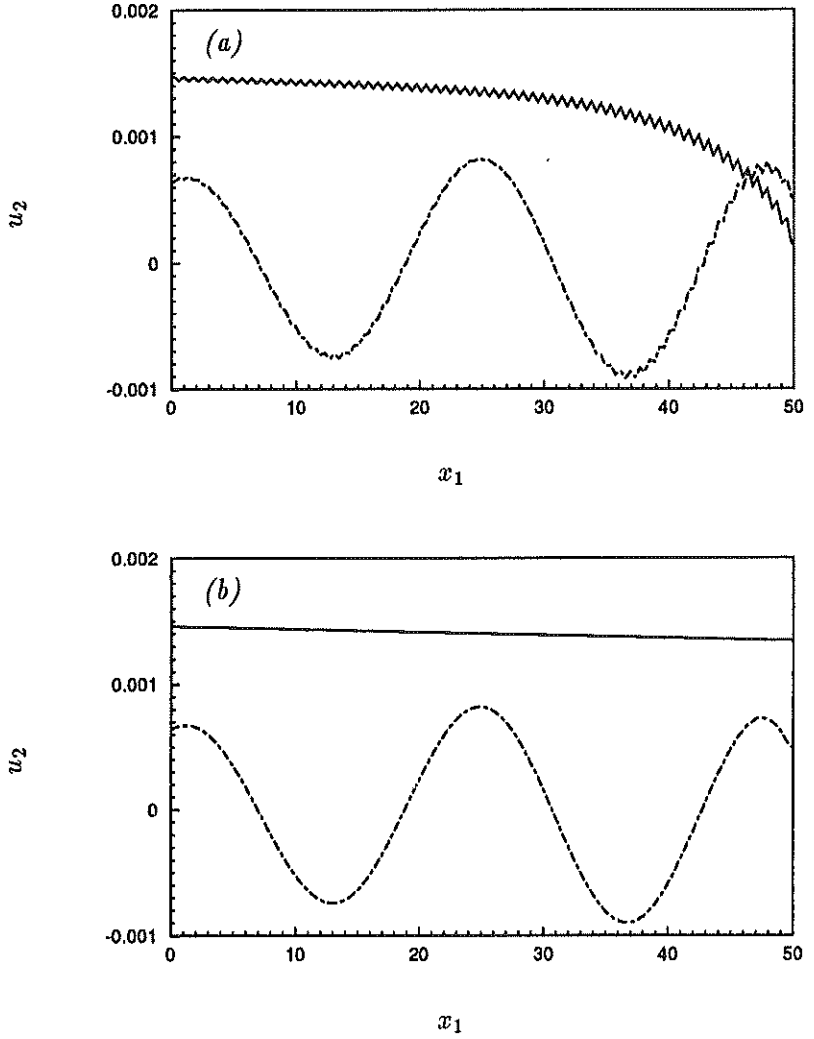

FIGURE 1. Streamwise distribution of mean (———) and disturbance (— - —) normal velocities at $x_2 = 3.1$, caused by T-S waves in a Blasius boundary layer. (a) is obtained using outflow condition (14), and (b) is obtained using (15) with a small buffer zone. The inlet Reynolds number $Re_0^* = 1000$.

has also been subjected to critical tests for linearly growing, small, two-dimensional disturbances. The computational results agree well with linear stability theory results in terms of both the eigenmode shape and the spatial amplification rate.

2.3 Preliminary results

2.3.1 2-D Tollmien-Schlichting waves

The first numerical experiment conducted deals with the sound field produced by

spatially amplifying, two-dimensional Tollmien-Schlichting waves. A 2-D version of (5) and (6) is solved using 514×66 grid points in a domain ($0 \leq x_1 \leq 200$, $0 \leq x_2 \leq 20$), where the spatial coordinates are nondimensionalized relative to the displacement thickness at the inflow boundary. The inflow Reynolds number based on the displacement thickness is $Re_0^* = 1000$.

After a steady flow field has been established, inflow velocities are disturbed at the least stable frequency corresponding to the 2-D eigenmodes described in (13). The T-S wave train so created exhibits linear or nonlinear characteristics, depending on the amplitude of boundary excitation, as demonstrated in Fig. 2. One notices that, in both cases, there is no appreciable distortion in the T-S waveform near the inflow/outflow boundary.

An attempt has been made to deduce the far-field sound emitted by the amplification and/or nonlinearization of T-S waves in the boundary layer. If the flow Mach number is very small (say, 0.01, as in marine applications), the computational domain can be considered as a compact source, and (11) is valid. Numerical integrations of (11) and (12) show basically harmonic density variations at the T-S wave frequency at a given far-field point $\vec{X}$. However, it is discovered that the amplitude of the sound signal alters dramatically when the front of the T-S wave train crosses the outflow boundary. Further numerical tests verify the existence of a strong, artificial boundary effect on the calculated sound level, which masks the true sound of flow instability. This arises not because of the numerical boundary condition treatment for the flow region, but rather due to the fact that the entire T-S wave train is not included in the finite computational domain. Based on (11), the calculated sound signal is determined by the time derivatives of the total Reynolds stress and surface viscous stress in the source region. In the present case since the source region has artificially defined open boundaries, the time variations of Q_{ij} and R_1 (cf. (12)) are caused primarily by T-S waves crossing the boundaries, rather than by their slow amplification within the region.

The situation is best illustrated by considering an isolated 2-D wave packet, instead of the entire wave series, as it traverses the the source region. The wave packet is generated by multiplying the 2-D mode in (13) by $\exp\left[-\left((t-210)/70\right)^2\right]$. The time history of the longitudinal quadrupole $\ddot{Q}_{11}$ (the double dots denote second time-derivative) computed from (12) is depicted in Fig. 3, which shows two distinct regimes of oscillations, one as the packet enters from the upstream boundary and the other as it exits at downstream. The effect of wave amplification and spreading is represented by the relatively quiet regime in-between. Similar behavior has been observed for $\ddot{Q}_{22}$ and $\dot{R}_1$. The unphysical boundary effect on sound calculation is probably exacerbated because of the compact source assumption. Non-compact sources (larger M) are acoustically more efficient, and the boundary effect is expected to become less predominant. Nonetheless, an accurate assessment of T-S wave generated sound is still impossible unless those artificial boundary effects are eliminated or adequately accounted for.

In view of the small effect of T-S waves on sound radiation, we decide to concentrate on a practically more important issue – the sound generated by a local

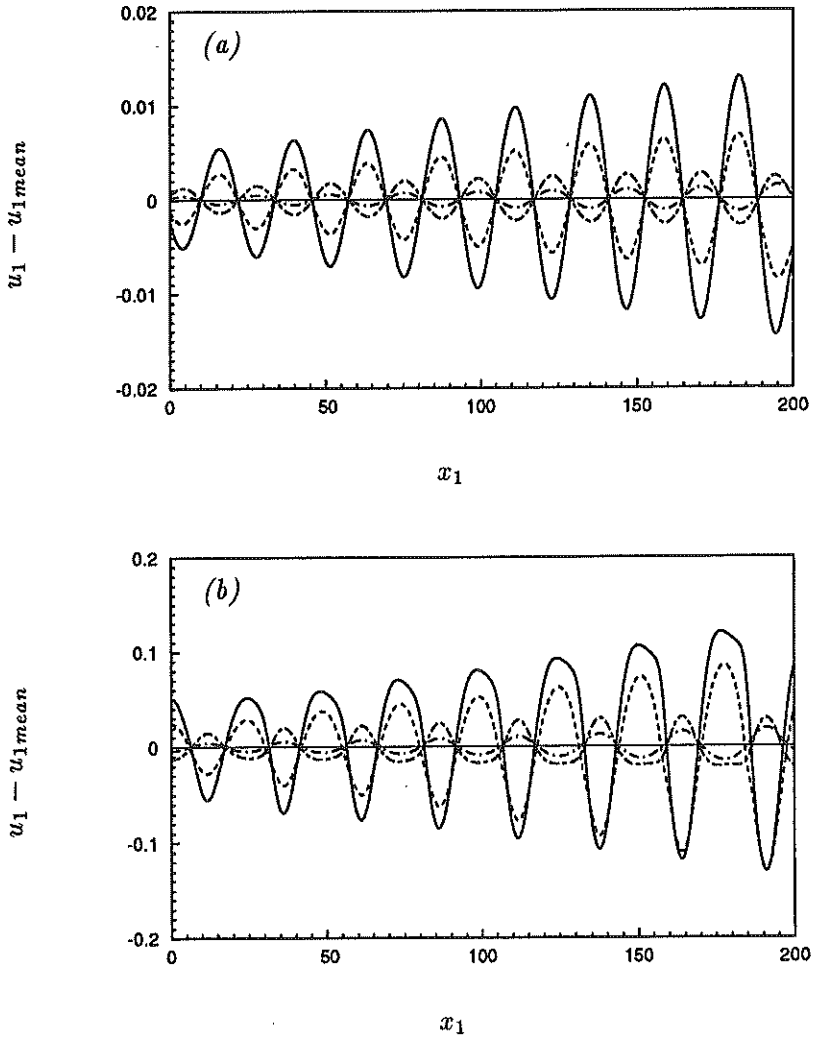

FIGURE 2. Streamwise disturbance velocity $(u_1 - u_{1mean})$ as a function of x_1 at four x_2-locations (—— $x_2 = 0.44$, - - - - $x_2 = 1.35$, — - — $x_2 = 3.02$, —·— $x_2 = 7.87$) in a Blasius boundary layer. The T-S waves are caused by a 2-D upstream excitation given in (13). (a) $\epsilon^{2D} = 0.005$, and (b) $\epsilon^{2D} = 0.05$.

breakdown of the laminar boundary layer.

2.3.2 3-D laminar breakdown

Simulations are under way for the three-dimensional development of boundary layer instability that leads to laminar breakdown of the fundamental type. In order to enhance grid resolution as well as to isolate the true acoustic source from boundary-induced artifacts, the eigenmode excitation described in (13) is multiplied by $\exp\left[-\left((t-80)/40\right)^4\right]$. This creates a perturbed flow region of limited streamwise

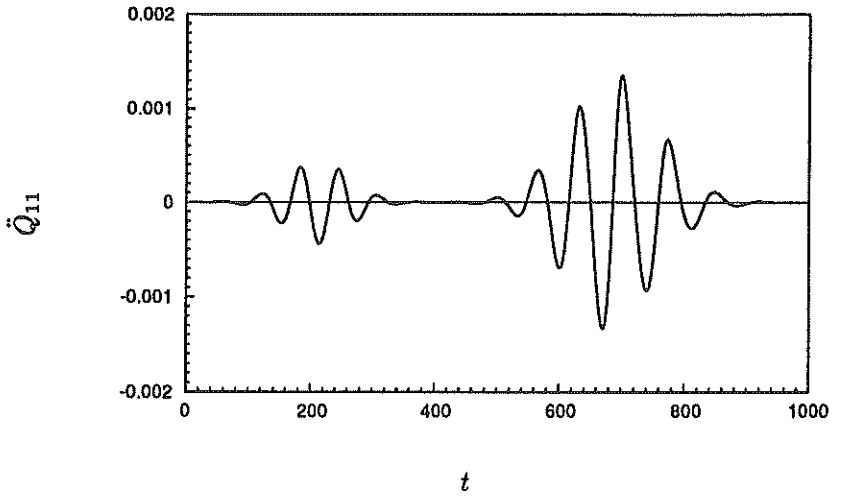

FIGURE 3. Longitudinal quadrupole $\ddot{Q}_{11}$ calculated using (12) for the case of a 2-D wave packet crossing the source region. The wave packet is created by disturbing the upstream boundary for a short time duration. $\epsilon^{2D} = 0.01$ and $\epsilon^{3D} = 0$.

extent, completely enclosed within the computational domain. Numerical experiments show that the isolated wave packet evolves in a way similar to that for regular T-S wave series in forced transition, at least up to the multiple spike stage.

The following parameters are employed in the simulation: $Re_0^* = 1000$, $\epsilon^{2D} = 0.025$, $\epsilon^{3D} = 0.01$, $\theta = 0$, $\phi = \pi/4$, and $\beta = 0.094$. The latter corresponds to the least stable frequency for 2-D T-S waves at inflow. Computations start out on a $514 \times 98 \times 66$ grid covering a physical domain defined in $0 \leq x_1 \leq 180$, $0 \leq x_2 \leq 20$ and $0 \leq x_3 \leq \lambda_z$, where $\lambda_z \approx 25.95$ is the spanwise wavelength. As a detached high shear layer appears in the peak x_1–x_2 plane (cf. Fig. 4a), the spatial resolution demand becomes increasingly severe for the unstable region as the secondary instability intensifies and higher instabilities develop. Meanwhile, the flow field for $x_1 < 50$ has become basically steady after the passage of the disturbance structure. Consequently, the inflow boundary is moved from $x_1 = 0$ to 50, and the solution is interpolated onto a refined grid of $1026 \times 98 \times 130$.

Results of the ensuing computation are exemplified in Figs. 4b–4d, which, like Fig. 4a, plot the spanwise vorticity contours in the peak plane. The spatial resolution requires further improvement. Nonetheless, these plots capture the essential features of the shear layer roll-up and the formation of one, two, and multiple spikes as time progresses.

Figs. 5 depicts time-variations of the quadrupole acoustic source terms $\ddot{Q}_{ij}$ calculated from (10), again under the compact source assumption. In the calculation, Lighthill's stress tensor is approximated by the Reynolds stress only; the viscous stress contribution, computed separately, is found to be a factor of 10^{-3} smaller. The time instants corresponding to the four snapshots depicted in Fig. 4 are marked

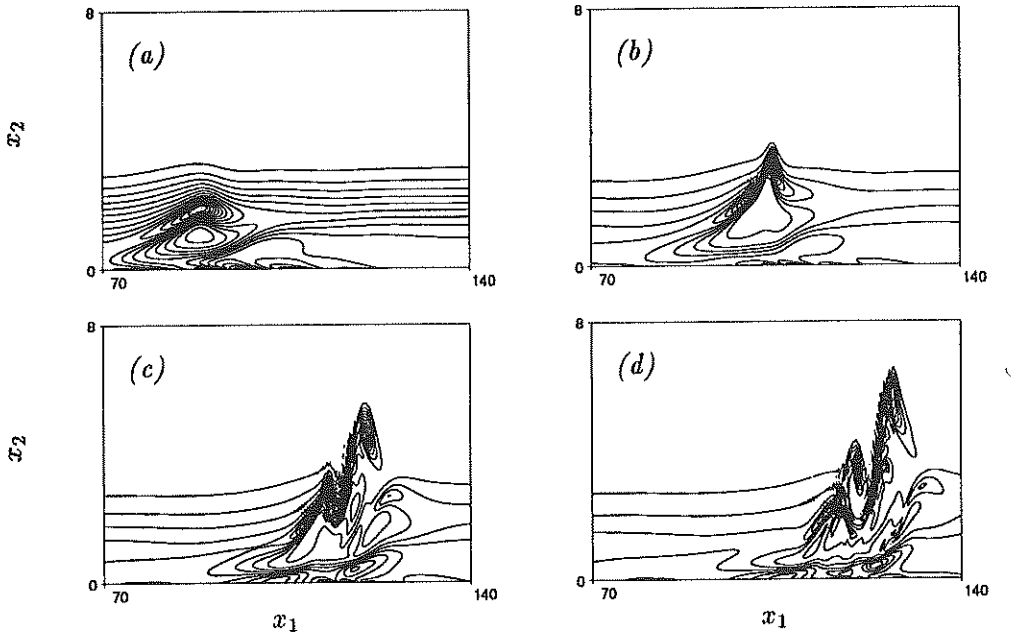

FIGURE 4. Instantaneous spanwise vorticity contours in the peak x_1–x_2 plane during breakdown of high-shear layer. (a) $t = 279$; (b) $t = 305$; (c) $t = 326$; and (d) $t = 335$.

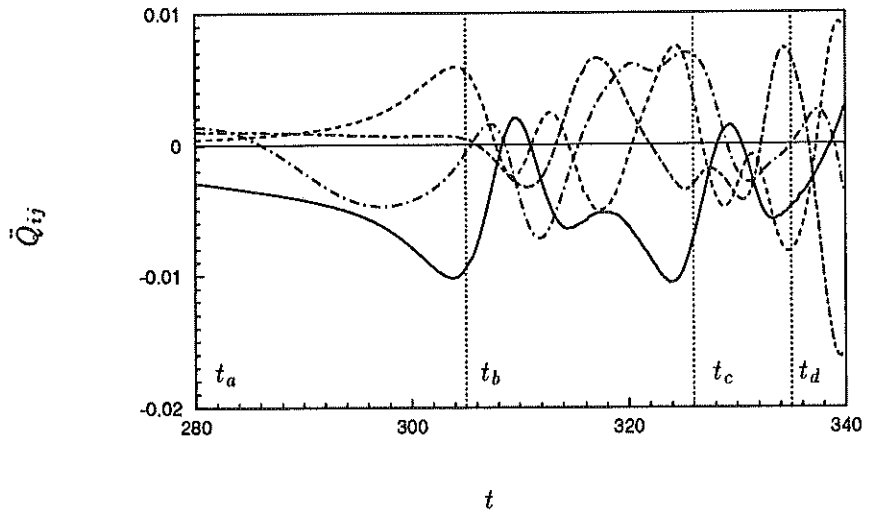

FIGURE 5. Quadrupole acoustic source terms (—— $\ddot{Q}_{11}$, ---- $\ddot{Q}_{22}$, —·— $\ddot{Q}_{33}$, —·— $\ddot{Q}_{12}$) calculated using (10) during high-shear layer breakdown. The time marks t_a, t_b, t_c and t_d correspond to the four snapshots in Fig. 4.

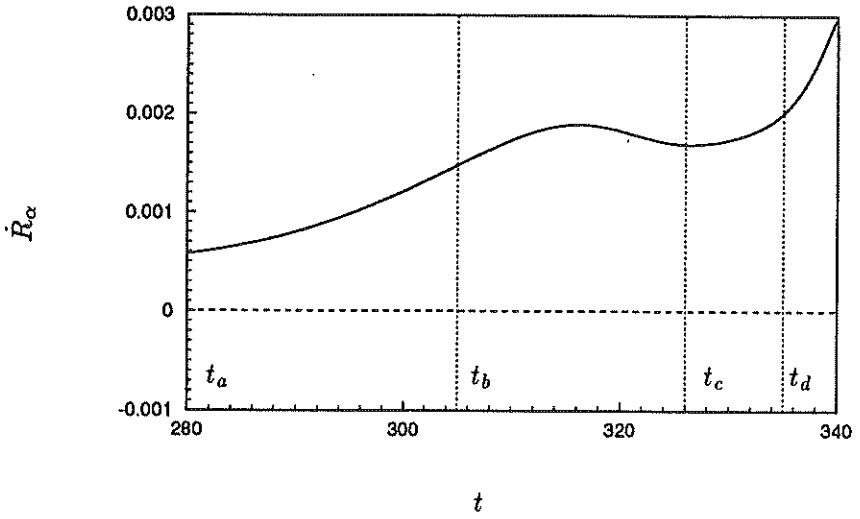

FIGURE 6. Surface dipole source (—— $\dot{R}_1$, ---- $\dot{R}_3$) calculated using (10) during high-shear layer breakdown. The time marks t_a, t_b, t_c and t_d correspond to the four snapshots in Fig. 4.

as t_a, t_b, t_c, and t_d in Fig. 5 for clear comparison. Due to symmetry with respect to the peak plane, $\ddot{Q}_{13}$ and $\ddot{Q}_{23}$ vanish. The other four source terms are seen to develop oscillations with higher frequency components relative to the basic T-S wave frequency (the T-S wave period ≈ 66.8). Apparently, these higher harmonics are associated with the roll-up of the detached high-shear layer. During the same time period, the surface dipole $\dot{R}_1$ calculated from (10) is still dominated by low frequency behavior, as demonstrated in Fig. 6. However, it is expected to rise in both frequency and amplitude as the shear layer near the wall intensifies. The other dipole, $\dot{R}_3$, is identically zero again due to symmetry.

Because of insufficient data and relatively poor resolution for the source flow simulation at the present stage, a more quantitative analysis of acoustic implications is deferred to future work.

3. Future plans

The first priority is to improve the accuracy of the source field computation by grid refinement and optimization so that reliable results for more advanced transition stages can be obtained. A nonuniform mesh in the streamwise direction should allow much better resolution in the region of intense shear without increasing the total number of grid points in that direction. As pointed out by Zang *et al.* (1989), resolution requirements for numerical simulations of transition are extremely severe, and inadequate resolution may result in less intense detached shear layers and premature roll-up.

Once an accurate source field is obtained, attention will be focused upon the radiated acoustic waves. We will analyze the sound characteristics and directivity

associated with specific source mechanisms during boundary layer transition, and we will identify the dominant contributors to the radiated sound field. The analysis will not be restricted to compact sources; a more general formulation based on (8) should be used to investigate the effect of non-compact source distributions.

In the long run, it would be of interest to study the sound of turbulent spots and to compare the results with those due to laminar breakdown. A more difficult extension of this work would be to include the coupling between the fluid motion and the vibration of an elastic plate. Such flow-structure interactions are often the dominant source of sound production and are, therefore, of great practical importance.

Acknowledgements

This work was produced in collaboration with Prof. S. Lele and Prof. P. Moin. We would like to thank Y. Na for assistance with the Navier-Stokes code, and S. Collis for providing the Orr-Sommerfeld eigensolver. Throughout this work, we have benefited from discussions with T. Colonius and B. Mitchell of the aeroacoustics group at Stanford.

REFERENCES

AKYLAS, T. R. & TOPLOSKY, N. 1986 The sound field of a Tollmien-Schlichting wave. *Phys. Fluids.* **29,** 685–689.

CRIGHTON, D. G., DOWLING, A. P., FFOWCS WILLIAMS, J. E., HECKL, M., & LEPPINGTON, F.G. 1992 *Modern Methods in Analytical Acoustics*, Chapt. 16. Springer-Verlag.

CROW, S. C. 1970 Aerodynamic sound emission as a singular perturbation problem. *Stud. Appl. Math.* **49,** 21–44.

FARABEE, T. M., HANSEN, R. J., & KELTIE, R. F. (eds.) 1989 *Flow-induced Noise due to Laminar-Turbulence Transition Process,* Symposium for ASME Winter Annual Meeting, San Francisco, 1989.

FASEL, H. F. 1990 Numerical simulation of instability and transition in boundary layer flows. In *Laminar-Turbulent Transition.* IUTAM Symposium, Toulouse, France, 1989 (Arnal, D. & Michel, R. Eds.), Springer-Verlag.

HAJ-HARIRI, H. & AKYLAS, T. R. 1986 Sound radiation by instability wavepackets in a boundary layer. *Stud. Appl. Math.* **75,** 57–76.

JOHANSSON, B. C. V. 1993 Boundary conditions for open boundaries for the incompressible Navier-Stokes equation. *J. Comp. Phys.* **105,** 233–251.

KLEISER, L. & ZANG, T. A. 1991 Numerical simulations of transition in wall-bounded shear flows. *Ann. Rev. Fluid Mech.* **23,** 495–537.

LE, H. & MOIN, P. 1991 An improvement of fractional step methods for the incompressible Navier-Stokes equations. *J. Comp. Phys.* **92,** 369–379.

LIGHTHILL, M. J. 1952 On sound generated aerodynamically; I. General theory. *Proc. Roy. Soc. London Ser. A.* **211,** 564–587.

MITCHELL, B. E., LELE, S. K., & MOIN, P. 1993 Direct computation of the sound from a compressible co-rotating vortex pair. *J. Fluid Mech.* Accepted for publication.

PAULEY, L. L., MOIN, P., & REYNOLDS, W. C. 1988 *A Numerical Study of Unsteady Laminar Boundary Layer Separation*, Report No. TF-34, Dept. of Mech. Engr., Stanford University.

TAM, C. K. W. & MORRIS, P. J. 1980 The radiation of sound by the instability waves of a compressible plane turbulent shear layer. *J. Fluid Mech.* **98**, 349–381.

ZANG, T. A. & HUSSAINI, M. Y. 1990 Multiple paths to subharmonic laminar breakdown in a boundary layer. *Phys. Rev. Lett.* **64**, 641–644.

ZANG, T. A., KRIST, S. E. & HUSSAINI, M. Y. 1989 Resolution requirements for numerical simulations of transition. *J. Sci. Comp.* **4**, 197–217.